sample quantity reduced by about half. Among the few nanotubes left behind in this twice-oxidized sample, the ratio of coated to uncoated tubes had increased dramatically (>80%). Observation of the tips of the remaining coated tubes showed that, in most cases, oxidation has preferentially etched the inner layers of the tube, leaving the outer coatings and few outer tube layers (Fig. 5*A*) and giving clearer views of the coated film through the enlarged tube centres. This contrasts with the oxidation behaviour of pure nanotubes, where the attack proceeds from the outside to the inside, leaving chisel-shaped tips.

A possible orientational relationship between the outermost tube-layer lattice and the coated film now becomes discernible in some cases (using electron diffraction; Fig. 5*B*), owing to the selective removal of most of the inner layers. The few remaining outer tube layers (Fig. 5*A*) produce a narrow angular spread for the (*hk*0) spots (~4°), and the approximate orientation of the outer carbon honeycomb lattice can be determined with respect to the tube axis. The orientation of the oxide lattice can be deduced from the visible V_2O_5 spots in the diffraction pattern. In this case the (001) V_2O_5 basal planes grow on the (001) graphite surface with a near-parallel coincidence for two sets of planes; the (100) graphite‖(110) V_2O_5, and (010) graphite‖(310) V_2O_5 (Fig. 5*B*, *C*). For the second set of planes the spacing mismatch (~20%) is in the range that could introduce van der Waals epitaxy[20,21] in the system, as observed in layered dichalcogenides and Langmuir–Blodgett films. This type of lattice alignment occurs between weakly interacting surfaces with no dangling bonds (on cleavage planes, as here).

After the second oxidation, we find that the sample contains mainly larger (micrometre-sized) oxide structures, which covered nanotube bundles initially but now show pure oxide composition and hollow morphology (from EELS mapping), all graphitic structures having been removed. There are many extremely thin oxide skins (typically 10–50 nm in width, up to few hundred nanometres long and <1 nm thick) left behind in the sample. We see a few cylindrical structures of dimensions typical of larger nanotubes (Fig. 5*D*) of pure V_2O_5 (verified by diffraction and EELS). The observed skins could have originated from discontinuous films on nanotubes or from continuous films broken during sonication. The nanofibrils of V_2O_5 are flexible and collapsible under electron irradiation. We also find some solid rod-like V_2O_5 structures with a morphology typical of the filling in tubes, typically 5–8 nm in diameter and a few hundred nanometres long. The results indicate that nanotube templates are partially removable and point to their possible use as degradable templates to fabricate new ceramic films having layered structures.

The ability to coat the unreactive graphite basal planes that make nanotube surfaces with thin V_2O_5 films increases the versatility of nanotubes, because V_2O_5 is a good building block for catalytic complexes by organic routes[22]. Coated conventional carbon fibres have found a variety of applications[23]. Coated and filled nanotube sandwich structures should have vastly different optical and electrical properties, and have better oxidation resistance (from our observations) than pure nanotubes. Vanadium pentoxide is an important catalyst[24] and a functional ceramic with uses ranging from batteries to switching elements[25,26] with properties depending closely on dimensionality and oxygen stoichiometry. There is a great industrial interest in growing thin films of different vanadium oxides[27]. Our results point to a new synthesis route for the fabrication of such thin-film ceramic nanostructures using nanotubes as efficient templates. □

Received 20 April; accepted 22 May 1995.

1. Ajayan, P. M. & Iijima, S. *Nature* **361,** 333–334 (1993).
2. Tsang, S. C., Chen, Y. K., Harris, P. J. F. & Green, M. L. H. *Nature* **372,** 159–162 (1994).
3. Guerret-Plécourt, C., Le Bouar, Y., Loiseau, A. & Pascard, H. *Nature* **372,** 761–765 (1994).
4. Iijima, S. *Nature* **354,** 56–58 (1991).
5. Ebbesen, T. W. & Ajayan, P. M. *Nature* **358,** 220–222 (1992).
6. Ajayan, P. M. *et al. Nature* **362,** 522–525 (1993).
7. Prasad, R. & Lele, S. *Phil. Mag. Lett.* **70,** 357–361 (1994).
8. Dujardin, E., Ebbesen, T. W., Hiura, H. & Tanigaki, K. *Science* **265,** 1850–1852 (1994).
9. Ikemiya, N., Umemoto, J., Hara, S. & Ogino, K. *ISIJ Int.* **33,** 156–165 (1993).
10. Amelinckx, S. *et al. Science* **267,** 1334–1338 (1995).
11. Galy, J. *J. Solid St. Chem.* **100,** 229–245 (1992).
12. Cava, R. J. *et al. J. Solid St. Chem.* **65,** 63–71 (1986).
13. Oshio, T., Sakai, Y. & Ehara, S. *J. Vac. Sci. Technol.* B**12,** 2055–2059 (1994).
14. Smith, R. L., Lu, W. & Rohrer, S. *Surf. Sci.* **322,** 293–300 (1995).
15. Cullen, S. L., Boothroyd, C. B. & Humphreys, C. J. *Ultramicroscopy* **56,** 127–134 (1994).
16. Ajayan, P. M. *et al. Phys. Rev. Lett.* **72,** 1722–1725 (1994).
17. Lin, X. W. *et al. Phys. Rev.* B**47,** 3477–3481 (1993).
18. Smith, D. J., McCartney, M. R. & Bursill, L. A. *Ultramicroscopy* **23,** 299–304 (1987).
19. Fan, H. J. & Marks, L. D. *Ultramicroscopy* **31,** 357–364 (1989).
20. Zasadzinski, J. A. *et al. Science* **263,** 1726–1733 (1994).
21. Ohuchi, F. S., Parkinson, B. A., Ueno, K. & Koma, A. *J. appl. Phys.* **68,** 2168–2175 (1990).
22. Gai, P. L. & Kourtakis, K. *Science* **267,** 661–664 (1994).
23. Dresselhaus, M. S. *et al. Graphite Fibers and Filaments* (ed. Cardona, M.) 238–243 (Springer, Berlin, 1988).
24. Krylov, O. V. *Catalysis by Nonmetals* (ed. Loebel, E. M.) (Academic, New York, 1970).
25. Scarminio, J. *et al. Electrochim. Acta* **38,** 1637–1642 (1993).
26. Kim, D. H. & Kwok, H. S. *Appl. Phys. Lett.* **65,** 3189–3191 (1994).
27. Shimizu, Y., Nagase, K., Miura, N. & Yamazoe, N. *Jap. J. appl. Phys.* **29,** L1708–L1711 (1990).

ACKNOWLEDGEMENTS. We thank P. Ballongue and C. Jeanguillaume for their help. P.R. acknowledges a grant from the DAAD (HSP-II).

Deflation of Mount Etna monitored by spaceborne radar interferometry

Didier Massonnet*, Pierre Briole† & Alain Arnaud‡

* Centre National d'Etudes Spatiales, 18 Avenue E. Belin, 31055 Toulouse, France
† Institut de Physique du Globe, 4 Place Jussieu, 75005 Paris, France
‡ Groupe CISI, 1 Rue des Cosmonautes, 31400 Toulouse, France

GROUND-BASED measurements of volcano deformation can be used to assess eruptive hazard, but require the costly (and often hazardous) installation and maintenance of an instrument network. Here we show that spaceborne radar interferometry, which has already shown its utility in mapping earthquake-related deformation[1], can be used to monitor long-term volcano deformation. Two families of synthetic aperture radar images, acquired from ascending and descending orbits by the satellite ERS-1, and looking at Mount Etna from opposite sides, cover the time period from 17 May 1992 to 24 October 1993, and include the second half of Etna's most recent eruption. Despite artefacts of the interferometric technique, we can observe a volcano-wide deflation, which is an expected consequence of the eruption, but which had not previously been appreciated. We quantify it using a simple model based on the change of pressure in a sphere located in an elastic half-space; the modelled deformation increases linearly with time until the end of the eruption. Our results show that it will be possible to use this technique to detect the inflation of volcanic edifices that usually precedes eruptions.

Mount Etna (Fig. 1) is one of the most active and best studied volcanoes in the world. The last eruption started on 14 December 1991 in the Valle del Bove, a large amphitheatre formed by collapse of the eastern flank. Lava was erupted along a fracture system that had opened in 1989[2], and covered most of the southern part of the Valle del Bove. The eruption stopped on 31 March 1993 after 473 days. The rate of lava production remained stable during most of the eruption, and the total erupted volume was $\sim 3 \times 10^8$ m^3 (ref. 3).

To measure the deformation, we constructed interference patterns from the difference of pairs of synthetic aperture radar (SAR) images acquired by the ERS-1 satellite. This geodetic technique can measure centimetre-size changes in the ground surface[1,4–6]. The resulting interferogram is a contour map of the change in range to the volcano surface, measured along the

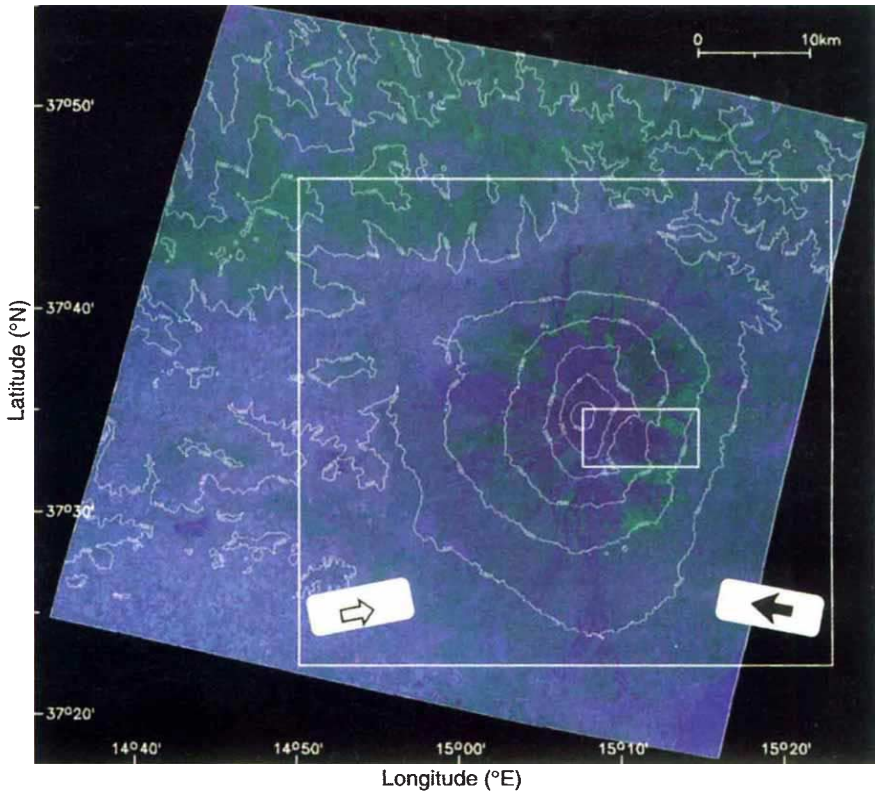

FIG. 1 Location map from a SPOT image, representing the limits of the digital elevation model used with ascending as well as descending radar images. The model has been computed by ISTAR S. A. (Valbonne, France) using two SPOT images acquired on 22 and 23 July 1991. Vegetation-covered areas appear in green and lava flows are dark. The radar antenna points roughly to the West in ascending orbits and to the East in descending orbits. Interferometric sensitivity to various ground displacements can be determined from unitary vectors pointing from Mount Etna towards the satellite in its ascending or descending orbits. These vectors, the Earth-surface projections of which are shown (outlined arrow, ascending; solid arrow, descending), are given explicitly as (0.418, −0.085, 0.904) for ascending orbits and (−0.373, −0.077, 0.925) for descending orbits in a coordinate set (east, north, up) on the Earth's surface. These satellite-directed vectors indicate roughly the same sensitivity of the two data sets to south–north or vertical displacements, but reveal opposite signs for east–west displacements. The values given above for the summit of Mount Etna. Their variations within the image frame and within a given family of orbits are very slight and can be neglected. The larger box outlined in white is the location of Figs 3 and 4. The area where local surface deformation can be seen in Fig. 3*a*, *e*, *h* and 4*a* is indicated by the smallest box.

direction towards the satellite. Each contour line, or fringe, represents 28 mm, or half the wavelength of the radar. Our approach requires two images and uses a digital elevation model to calculate and remove the effect of topography. For this study we used a digital elevation model of the area accurate to 8 m (r.m.s. error), according to its technical documentation (ISTAR, Valbonne, France). The model has been obtained using data from the optical remote-sensing satellite SPOT. The accuracy of the measurement is limited mostly by atmospheric progragation heterogeneity and residual topographic contributions. Propagation heterogeneity introduces errors that are generally less than half a fringe, but which may be as large as three fringes locally, in exceptional conditions. A pair-wise logic allows their identification as tropospheric or ionospheric artefacts[7]. Residual topographic errors depend on the separation of the two orbits: the smaller the separation, the lower the sensitivity to topography and any residual topographic errors. An interferogram is characterized by the time interval it spans and by its altitude of ambiguity[8], equal to the amount of elevation change that produces one topographic fringe. The altitude of ambiguity is roughly inversely proportional to the orbital separation.

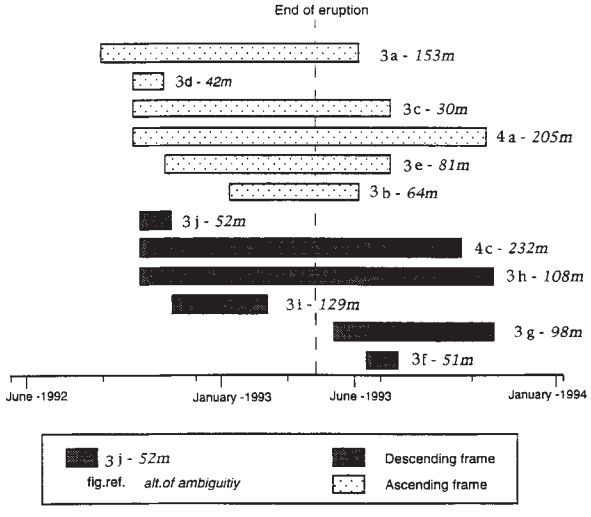

FIG. 2 Bar chart of the interferometric pairs shown as figures in this study. Ascending pairs are represented by dotted bars, descending pairs by shaded bars. The numbers on the right-hand side of each bar are the figure code of the interferograms and the altitude of ambiguity.

The ERS-1 satellite acquired 13 radar images of Mount Etna during ascending orbits (travelling north), looking roughly to the east during the night (23:16 local time). It also acquired 16 radar images during descending orbits (travelling south), looking roughly to the west during the day (11:40). Only images from the same family of orbits can be combined. The ascending (descending) images give 78 (120) potential interferometric combinations. We selected 32 ascending and 60 descending combinations with altitudes of ambiguity larger than 20 m, thus ensuring negligible residual topographic contribution. About 30 interferograms presented enough coherence to be analysed and 12 of them contributed quantitatively to the present study. Their features are summarized in Fig. 2.

Experience with this large interferometric data set has led to three general conclusions: on average the interferograms made from ascending (night-time) passes are better than those from descending passes, possibly owing to more stable atmospheric conditions and a more quiescent vegetation state; interferogram phase changes due to ionospheric or tropospheric propagation effects[7] are common and must be identified to avoid displacement errors of up to one fringe, or 28 mm (Fig. 3*d*, *e*, *h*, *i*); and the coherence between images does not decrease systematically with time. Fig. 4*a* shows one of the best ascending interferograms, obtained over 385 days. The image is dominated by four concentric fringes that suggest an ~11-cm deflation of the whole volcano. Localized fringes are also visible in the Valle del Bove and show local subsidence, well correlated with the 1989 lava

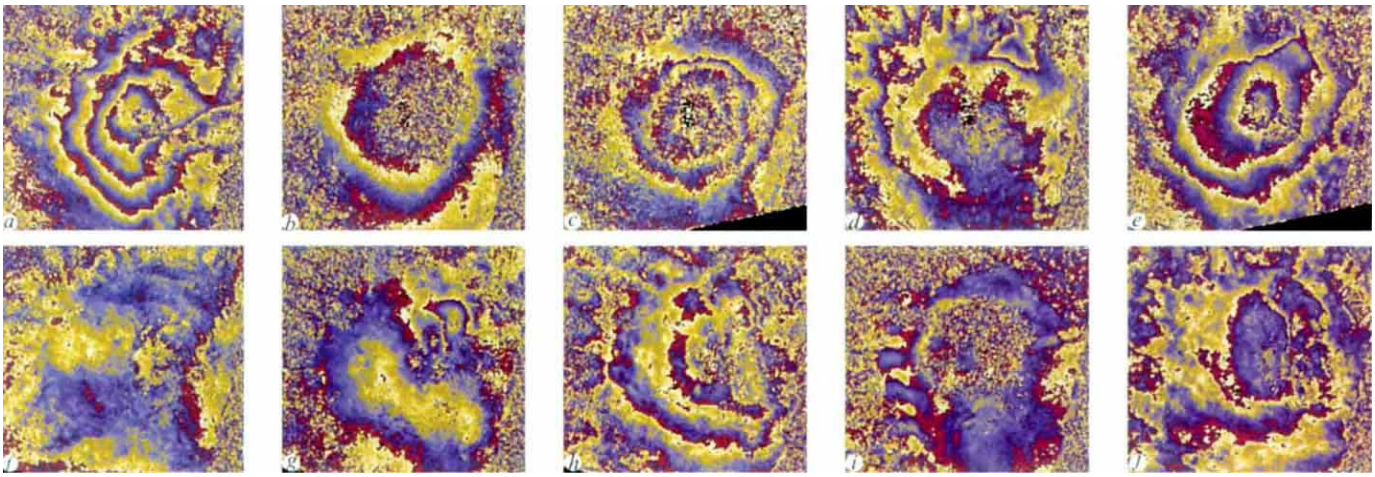

FIG. 3 Examples of interferograms (*a*–*e*, ascending orbits; *f*–*j*, descending orbits). *a*–*c* Show the subsidence of the volcano at different stages. The triangular feature in *d* and *e* is related to the ascending orbit of 1 December 1992, and is equivalent to a positive displacement of 3 cm. It does not appear in the interferogram 3c and is thus produced by a reversible source. This feature also does not appear in interferogram *j* that is made from images taken on 4 October and 8 November 1992. The most likely cause is thus an ionospheric propagation heterogeneity[7]. Interferogram *f* (35 days separation, starting three months after the end of the eruption) shows good coherence and not a single fringe despite a relatively small altitude of ambiguity (51 m). It was used to assess the quality of the digital elevation model and thus to calibrate the maximum expected topographic residual on the other interferograms. Examples of tropospheric hetrogeneities are shown in *h* (semicircular feature different from a closed fringe) and *i* (chained 'clouds' on the left-hand side).

field. Such phenomena have been observed on Etna by Murray[9] near recent lava flows, and can be interpreted as compaction of the fresh unconsolidated lava flow and downward flexure around it. The same subsidence is visible on the interferograms shown in Fig. 3*a* and *e*.

Deflation is not observed on the interferograms formed by images acquired after the end of the eruption, such as Fig. 3*f*. This interferogram is uniform in the areas where coherence is kept. Because its altitude of ambiguity is 51 m, we expect at most one-sixth of a cycle of topographic residual from the 8 m credited accuracy of our elevation model, which is clearly the case here. Such a topographic residual would account for less than 1/25 of a fringe, or 1 mm, in an interferogram with an altitude of ambiquity of 205 m, as Fig. 4*a*. Similarly, the fringes in Fig. 4*a* cannot be due to atmospheric propagation heterogeneities attached to one image, as the almost synchronous interferogram Fig. 4*c* shows a deflation of similar amplitude although formed with two images from descending orbits, which could

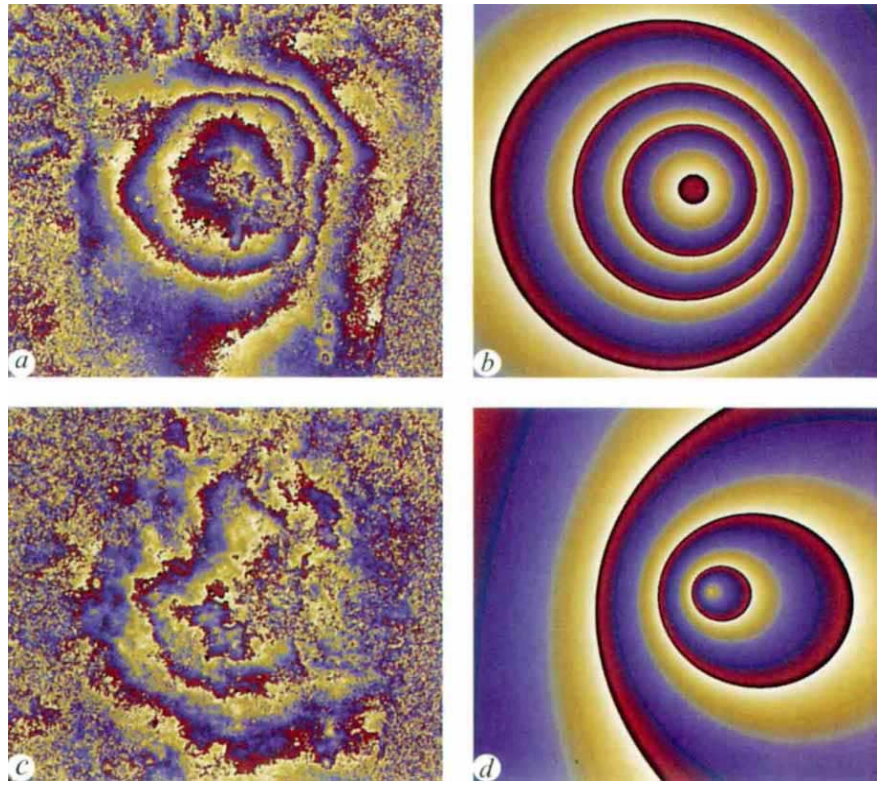

FIG. 4 Actual and modelled fringe patterns for the best ascending and the corresponding descending interferograms. One cycle of colour corresponds to a 28-mm change in range. About four fringes are visible in *a*, indicating a subsidence of the volcano. The interferogram corresponding to the best-fit model is shown in *b*. An almost synchronous descending interferogram is shown in *c*, and *d* is the interferogram for the best-fit model. The best fit is obtained with a source located 2 ± 0.5 km east of the centre cone and at 16 km depth.

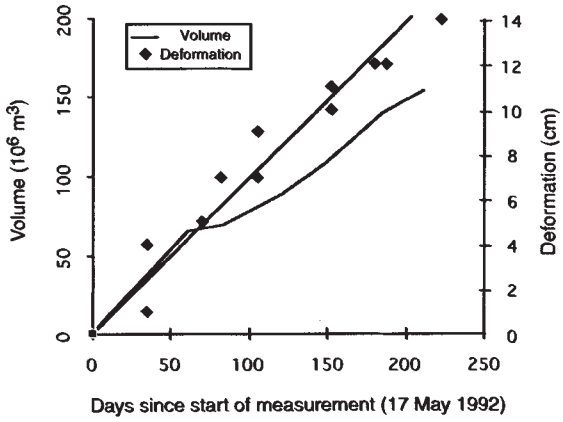

FIG. 5 Subsidence of the summit of Etna deduced from our data and plotted (diamonds and associated straight-line fit) as a function of the effective elapsed time. Volume of lava produced during the eruption (other solid line) as inferred from the field measurement[3]. Because no deformation is visible after the end of the eruption (Fig. 3*f*), the effective elapsed time was defined as the number of days that separate the first day of the interferogram and the last day of the interferogram or the last day of the eruption if earlier (Fig. 4). The error on the individual measurements is ≤1 cm, based on the quality of the model fit, assessed at intervals of 1 cm. Interferograms that did not provide an unambiguous fit at the 1-cm confidence level were not included in the quantitative study.

not have been affected by the same atmospheric propagation heterogeneities.

Assessing the deformation just by counting the fringes is difficult for several reasons. First, an interferogram does not give an absolute indication of phase and the background phase is difficult to assess. Second, the volcano-wide deflation pattern is obscured in areas where coherence is poor, such as some vegetion-covered areas and the summit, which freezes at times. The phase is also biased by local deformation and atmospheric artefacts. Thus, we separated the contribution of volcano-wide deflation by fitting the interferograms with a calculated theoretical displacement field derived from a simple model of pressure change in a sphere located in an elastic half-space[10]. The model, which also gives the total volume change, depends on four parameters: the coordinates of the centre of the sphere and the maximum amplitude of the displacement above this centre. In this model, we prescribe only changes of volume at depth, regardless of the consequences in terms of pressure, which would require knowledge of the size and rigidity of the source.

We used the ascending interferogram Fig. 4*a*, in combination with the best descending interferogram Fig. 4*c*, to fix the centre of the sphere. Its horizontal location was obtained by ascertaining the best fit of the centroids of the fringes for the data (Fig. 4*a* and *c*) to those for the models (Fig. 4*b* and *d*). The best fit was obtained with the centre of the sphere located 2 ± 0.5 km east of the central cone of Etna.

The maximum amplitude of subsidence in the interferogram shown in Fig. 4*a* was obtained by minimizing the residuals for a range of assumed depths of the sphere (10–20 km). The sensitivity of the solution to the depth is low, and our best fit was always obtained with a subsidence of 12 cm. This value is well constrained, in particular by the western and the southern parts of the image. We estimate the uncertainty in this value to be of the order of 1 cm. For the depth of the sphere, the best fit is not sharply defined, and is obtained between 13 and 19 km. We thus estimate the depth of the source to be 16 ± 3 km. We emphasize that our model does not constrain the location of the magma reservoir(s) beneath Etna or its finite shape, except that the model is consistent with a source at mid-crustal levels—deeper than anticipated from previous interpretations[11,12] based on measurements that did not sample the entire deformation field.

When modelling additional interferograms, we did not have to change the location of the centre of the sphere, but simply to adjust the maximum displacement, which indicates the geometric consistency of the model. For each interferogram we computed 20 residual images obtained by increasing the amplitude from 0 to 19 cm by steps of 1 cm and selected the minimum. We retained the 12 interferograms for which this choice was unambiguous at the 1-cm confidence level.

Figure 5 shows the maximum displacement (right-hand ordinate) plotted as a function of time, until the end of the eruption. These values are consistent whether obtained from ascending or descending interferograms, despite the very different sensitivity of the two families of data to east–west displacements, as explained in Fig. 1. This further confirms the geometrical consistency of the model. No deformation is measured after the end of the eruption, as shown by the interferogram in Fig. 3*g*. During the last seven months of the eruption sampled by our data, the maximum subsidence increases linearly at a rate of 21 mm per month. From GPS data, the subsidence of the volcano for the first five months of the eruption (inferred from the difference between data for July 1990 and June 1992) has been estimated[11] as 19 cm at the summit and 6–8 cm at points located 6–10 km from the top. Assuming that all the observed displacement occurred during the five months of eruption, the average rate of subsidence was 31 mm per month. The maximum horizontal strain rate predicted by our model is −0.9 p.p.m. per month for opposite points located at 11 km from the top, a value close to the −0.75 p.p.m. per month obtained earlier in the eruption[11].

The constant value of our subsidence rate is consistent with the stable rate of lava production measured in the field[3] and plotted in Fig. 5. The rate of volume change at the surface of the volcano deduced from our observation is 3.4×10^7 m^3 per month. This rate is not balanced by the production of lava (1.9×10^7 m^3 per month).

This analysis of data from Mount Etna validates the use of radar interferometry for volcano monitoring. Volcano-wide surface deformation is revealed and the associated volume change can be measured. The simplicity of our model allowed us to use many interferograms, even those of low quality—a practice further justified by the consistency of the amplitudes of subsidence. This technique could be used for surveying other active volcanoes, using existing (ERS-1 and J-ERS1) or future (ERS-2 and Radarsat) radar systems. Continuing work on other volcanoes, such as an unpublished study that we have initiated of Merapi volcano (Indonesia), shows that it is possible to obtain coherent images even in equatorial areas, where rapid surface changes occur owing to lush vegetation. □

Received 21 December 1994; accepted 5 May 1995.

1. Massonnet, D. *et al. Nature* **364**, 138–142 (1993).
2. Villari, L. (ed.) *Acta vulcanol.* **4**, 1–177 (1994).
3. *Global Volcanism Network* Smithsonian Inst. Bull. **16**(17)–**18**(5) (1991–1993).
4. Goldstein, R. M., Engelhardt, H., Kamb, B. & Frolich, R. M. *Science* **262**, 1525–1530 (1993).
5. Zebker, H. A., Rosen, P., Goldstein, R. M., Gabriel, A. & Werner, C. L. *J. geophys. Res.* **99**, 19617–19634 (1994).
6. Feigl, K. L., Sergent, A. & Jacq, D. *Geophys. Res. Lett.* (in the press).
7. Massonnet, D. & Feigl, K. L. *Geophys. Res. Lett.* (in the press).
8. Massonnet, D. & Rabaute, T. *IEEE Trans. Geosci. Rem. Sensing* **31**, 455–464 (1993).
9. Murray, J. B. *J. Volcanol. geotherm. Res.* **35**, 121–139 (1988).
10. Mogi K. *Bull. Earthquake Res. Inst. Tokyo* **36**, 34–134 (1958).
11. Nunnari, G. & Puglishi G. *Acta vulcanol.* **4**, 101–107 (1994).
12. Bonaccorso, A., Velardita, R. & Villari, L. *Acta vulcanol.* **4**, 87–96 (1994).

ACKNOWLEDGEMENTS. We thank L. Gray, P. Segall, G. Wadge and A. Bonaccorso for their helpful comments and suggestions. More than half of the ERS-1 scenes used in this study were provided free of charge by the European Space Agency. This study was partially funded by the Natural Risk Reduction Program of the European Community.